Taylor bubble formation and flowing in a straight millimetric channel with a cross-junction inlet geometry Part II: Gas-liquid mass transfer

Mei Mei, Claude Le Men, Karine Loubière, Gilles Hébrard, N. Dietrich

Taylor bubble formation and flowing in a straight millimetric channel with a cross-junction inlet geometry

Part II: Gas-liquid mass transfer

Mei Mei[1,2,3], Claude Le Men[1,3], Karine Loubière[2,3], Gilles Hébrard[1,3],

Nicolas Dietrich[1*,3]

[1] Toulouse Biotechnology Institute, Université de Toulouse, CNRS, INRAE, INSA, Toulouse, France

[2] Laboratoire de Génie Chimique, Université de Toulouse, CNRS, INP, UPS, Toulouse, France

[3] Fédération de Recherche FERMAT, CNRS, Toulouse, France

*Corresponding author: Dr. Nicolas Dietrich

E-mail: nicolas.dietrich@insa-toulouse.fr

Abstract

Using the resazurin-based colorimetric technique and advanced image acquisition, the equivalent oxygen concentration fields inside the liquid slugs were measured during and after the bubble formation stage at a cross-junction in a straight millimetric channel. Firstly, two different mechanisms were identified for the development of oxygen concentration fields depending on the two-phase Reynolds numbers (Re_{TP}). Under low Re_{TP}, a jet-like central oxygen concentration 'finger' occurred between the newly formed bubble and the gas finger at the bubble pinch-off point. Right after the bubble pinch-off, the dissolved oxygen was transported first by the entering liquid from two side inlets, and later by the developing recirculation loop inside the liquid slug. Under higher Re_{TP}, two highly concentrated oxygen concentration spots were formed near the bubble rear and the channel wall region, and a much more complex flow structure in the liquid slug appeared. Then, whatever the operating conditions, it was observed that the averaged oxygen concentrations inside the liquid slug followed a nearly linear relation as a function of the axial position in the channel, and that the related mass flux density decreased as far as the bubbles flowed along the channel's length. The bubble formation process could be decomposed into three stages when considering the temporal evolution of the cumulated oxygen mass and depending on the development of the liquid slug. At last, the overall volumetric liquid side mass transfer coefficients ($k_L a$) were deduced from the concentration fields, and found to linearly increase with the recirculation frequencies, leading to a scaling law.

Keywords: Bubble formation, cross-junction, Taylor bubbles, mass transfer, concentration fields

1. Introduction

Microstructured continuous-flow technology is now considered as one of the effective approaches for process intensification and gained many interests for a wide range of applications (Geng et al., 2020; Liu et al., 2020; Yan et al., 2021), especially for multiphase reactions (e.g., hydrogenation and (photo)oxidation). They could indeed offer several advantages compared to conventional batch processes, such as the enhanced heat and mass transfer rates, narrow residence time distribution, high exchange surface areas, and higher yields and selectivity (Willms et al., 2019; Mariotti et al., 2020; Xu et al., 2021; Yang et al., 2022).

Numerous experimental works (Butler et al., 2016; Yao et al., 2021) were devoted to investigating hydrodynamics (Roudet et al., 2011; Mei et al., 2020a; Xu et al., 2021) and mass transfer (Yang et al., 2017; Abiev, 2020; Kexel et al., 2021; Schlüter et al., 2021) under reactive conditions (Kastens et al., 2017; Paul et al., 2018; Krieger et al., 2019; Haase et al., 2020) for gas-liquid flows in confined geometries, especially for the Taylor flow regime. But most of them were limited to an overall evaluation of the mass transfer characteristics, making it difficult to separate contributions between the bubble formation and the bubble flowing stages. For example, recent works (Zhang et al., 2015; Zhang et al., 2018; Mei et al., 2020b; Liu et al., 2021; Zhao et al., 2021) have shown that the liquid side mass transfer coefficient decreased along the microchannel, namely that the mass transfer rates during bubble formation stage were relatively greater than the ones during bubble flowing stage. Therefore, there is a need to develop local measurements enabling simultaneous visualization of both hydrodynamics and mass

transfer during the first moments of the Taylor flow, namely when the bubbles are forming and detaching at the inlet.

The bubble formation process is a key point when designing microreactors because the question of "when and how bubble pinch-off happens" directly determines the bubble size, frequency and flow regimes (Dang et al., 2013), and thus the mass transfer characteristics. This has been then extensively investigated through experiments, simulations and theoretical analysis methods (Fu and Ma, 2015; Svetlov and Abiev, 2021). Although the physical properties (density ratio, viscosity ratio and surface tension, etc.) of gas-liquid and liquid-liquid systems are different, the bubble and droplet formation stage in microchannels could be both described by the filling and squeezing stages (Garstecki et al., 2006; Yao et al., 2021). However, it is surprising to remark that few works aims at understanding the role of the bubble formation stage into the overall gas-liquid mass transfer process occurring in Taylor flows (Yang et al., 2016a). Sun and Cubaud (2011) investigated the initial shrinkage of dissolved CO_2 bubble right after the bubble formation within several liquid pairs (e.g., water, methanol, and ethanol) and found that it was governed by the ratio of the diffusion coefficient and Henry's law constant. In the case of the absorption of CO_2 in NaOH, Tan et al. (2012) showed that the mass transfer coefficient k_L during the bubble formation stage could vary from 1.4×10^{-4} to 5.5×10^{-4} m s^{-1} depending on the gas and liquid flow rates and on the intersection angles at the inlet. The intensification factor of experimental k_L compared to that calculated according to the Higbie penetration diffusion model (Higbie, 1935) were identified between 5 and 15, resulting from efficient surface renewal and acceleration of gas phase. Based on the variation of bubble length (due to the fast consumption of CO_2 by the chemical reaction), the absorption fraction of the bubble

formation stage to the overall mass transfer could reach up to 40%. Later, Yao et al. (2014) and Yao et al. (2015) found a lower absorption fraction (from 1.5% to 10%) for CO_2 and water (or ethanol solution), which could be due to elevated pressure, lower bubble formation time and lack of chemical reaction in their system. On the contrary, Yang et al. (2016a) quantified a large contribution (45-90%) of the bubble formation stage on mass transfer when compared to the overall bubble flowing stage. Therefore, there is no consensus on the role of the mass transfer occurring during the bubble formation stage as strongly dependent on the fluid pairs, pressure, or flow rates.

In parallel, other researchers (Fries and Rohr, 2009) specifically investigated the effects of inlet geometry on mass transfer, and showed that a carefully designed inlet geometry could enhance mass transfer by varying unit cell lengths (2 to 8 times of the channel width). Sattari-Najafabadi et al. (2017) designed three kinds of inlet geometries (e.g., cross-shaped junction, cross-shaped T-junction and T-junction), and observed significant differences in terms of mass transfer during the droplet formation stage, depending on the junction configuration. In particular, the cross-shaped junction presented the best performances (also observed by Xu et al. (2008)) and could achieve up to 30% on the enhancement of overall $k_L a$, Soh et al. (2017) simulated the evolution of dissolved CO_2 in the liquid slug (silicone oil) by the VOF method and obtained the concentration fields inside the liquid slug during the bubble formation process inside a cross-junction. They divided the bubble formation process into the filling and squeezing stages and found that a majority of dissolved CO_2 were firstly carried by the liquid phase in the filling stage and then accumulated significantly during the squeezing stage due to the block of the liquid. However, the experimental measurements of the concentration fields during bubble formation process remains challenging and only few studies were

reported (Yang et al., 2016a). For example, by applying the micro PLIF technique, Bai et al. (2016) succeeded to measure the mass transfer process during the droplet formation and flowing stages, and calculated the associated volumetric mass transfer coefficients. They obtained relative higher values at the droplet formation stage than those at the droplet flowing stage. But so far, to the best of author's knowledge, there remains a research gap for quantitatively studying the mass transfer process during the filling and squeezing stages of the bubble formation.

In keeping with this context, the Part II of the present work aims at analyzing the mass transfer during the bubble formation process at a cross-junction and after the bubble detachment (flowing stage). This analysis will be drawn on the knowledge of the related bubble dynamics and the hydrodynamics features (flow regimes, pinch-off pattern, bubble and liquid slug lengths and velocities, etc.), that were detailed in the Part I of this work. The resazurin-based colorimetric method will be implemented to measure the transfer of oxygen from the bubble to the liquid phase. Section 2 will describe the experimental setup, the image processing, and the calibration method for mass transfer. In sub-section 3.1, the equivalent oxygen concentration fields during the bubble formation and flowing stages will be analyzed. The variations of average oxygen concentrations and mass flux density as a function of the axial position in the channel will be presented in sub-section 3.2, while the enhancement factor induced by the colorimetric chemical reaction will be estimated in sub-section 3.3. Then, the temporal evolution of the oxygen mass during the development of liquid slug at the bubble formation will be followed, revealing the occurrence of three stages (sub-section 3.4). At last, the relationship between the overall volumetric liquid side mass transfer coefficients $k_L \cdot a$ and the recirculation frequencies will be pointed out to propose a

scaling law (sub-section 3.5) that allowed gathering the database obtained in this work and other works from the literature.

2. Materials and methods

2.1 Experimental setup

The schematic experimental setup is described in detailed in Part I. Only the major information will be thus reported in this part. The gas phase (i.e., air) was fed from house compressed air lines and the flow rate was controlled by a DPC17S-V0L6-BB5 airflow controller. Liquid solutions were supplied by the syringe pump (Harvard Apparatus, PHD 22/2000, USA). The way to introduce gas and liquid phases into the main channel through a cross-junction is indicated in Fig. 1. The channel was lighted by a M530L4 LED and gas-liquid flow images were recorded by a Basler acA1920-155µm camera equipped with a 50 mm 1:1.4 Nikkor lens. The image acquisition frequency was set at 400 fps. The width, w_h, and depth, w_v, of the main channel were 2.19 mm and 2.13 mm, respectively. The hydraulic diameter of the channel, d_h (see Part I), was 2.16 mm.

Using a specific sliding support design, the camera could be horizontally changed to different region-of-interest (ROI) positions (see Fig. 1). This allowed investigating the mass transfer during the bubble formation stage, but also after the bubble detachment (flowing stage). Note that (i) some of the observing positions (from X_6 to X_{11}) were particularly selected to maintain the same flowing time while varying

the total superficial velocity for two-phase flow and (ii) X_i represented the starting position of the ROI window.

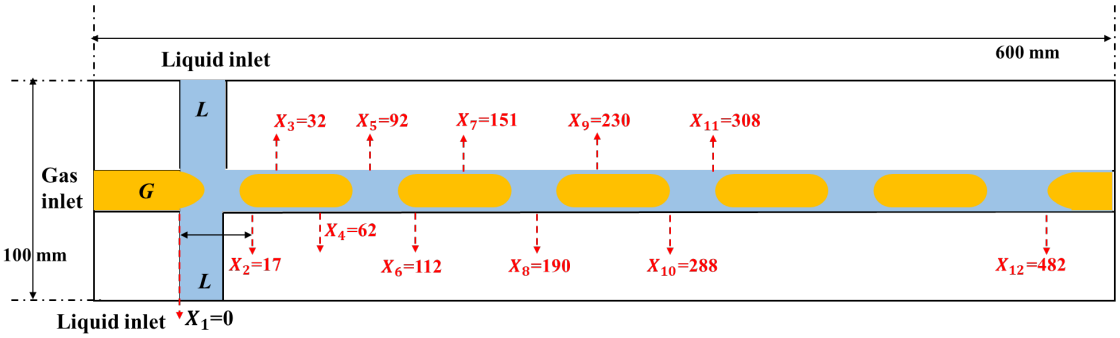

Fig. 1 Geometry of the straight milli-channel with a cross-junction. The 12 axial positions, X_i (expressed in mm), showing the region-of-interest (ROI), are marked by the red arrows. At $X_1 = 0$, the two phases enter in contact.

2.2 Resazurin-based colorimetric method

The colorimetric technique proposed by Dietrich et al. (2013) was implemented. The overall scheme of the redox reactions was as follows: in the presence of glucose and sodium hydroxide, resazurin (blue and not fluorescent) was first irreversibly reduced to resorufin (noted RF, pink and highly fluorescent, molecular mass of 213.19 $g \cdot mol^{-1}$), which was reversibly reduced to dihydroresorufin (noted DH, colorless, not fluorescent, and highly reactive with oxygen to form RF). The liquid phase was composed of D-glucose anhydrous (Sigma Aldrich, CAS 50-99-7, noted GL) at a concentration of 20 $g \cdot L^{-1}$, sodium hydroxide (Sigma Aldrich, CAS 1310-73-2) at a concentration of 20 $g \cdot L^{-1}$, and resazurin (Sigma Aldrich, CAS 199303, purity 93%, noted RZ) at a concentration of 74 $mg \cdot L^{-1}$ (considering purity). Therefore, the

maximal equivalent oxygen concentration, C_{max}, that could be measured by the resazurin-based method, was equal to 5.2 $mg \cdot L^{-1}$, calculated as follows.

$$C_{max} = \frac{[RZ] \cdot M_{O_2}}{2 \cdot M_{RZ}} \quad (1)$$

where M_{O2} (32 $g \cdot mol^{-1}$) and M_{RZ} (229.19 $g \cdot mol^{-1}$) were the molar masses of O_2 and resazurin, respectively. [RZ] was the mass concentration of resazurin, in $mg \cdot L^{-1}$.

2.3 Establishment of the calibration relationship

The calibration relationship linking the equivalent dissolved oxygen concentration and the gray level intensity (or absorbance) should be first established. For that, five aqueous solutions at different RZ concentrations (purity being considered) were prepared: 0, 9, 19, 37, and 74 $mg \cdot L^{-1}$ (the concentration of glucose and NaOH were kept at 20 $g \cdot L^{-1}$). Once prepared, air was injected inside these solutions to fully convert DH (colorless) into RF (pink). A portable dissolved oxygen probe (HQ40d) was used to verify that a fully conversion was reached with excess dissolved oxygen. Then, the "fully converted" solutions (pink) were immediately injected into the millimetric channel. For each RF concentration, 200 frames containing solution without RF or "fully converted" solution were taken, as shown in Fig. 2 (a). This process was repeated three times to reduce experimental uncertainties. At last, for each RF concentration, a time-averaged gray level value image was obtained, allowing to eliminate the slight deviation between instantaneous gray values. Note that this calibration procedure was made again each time when the ROI position (i.e., axial position, X_i) was changed.

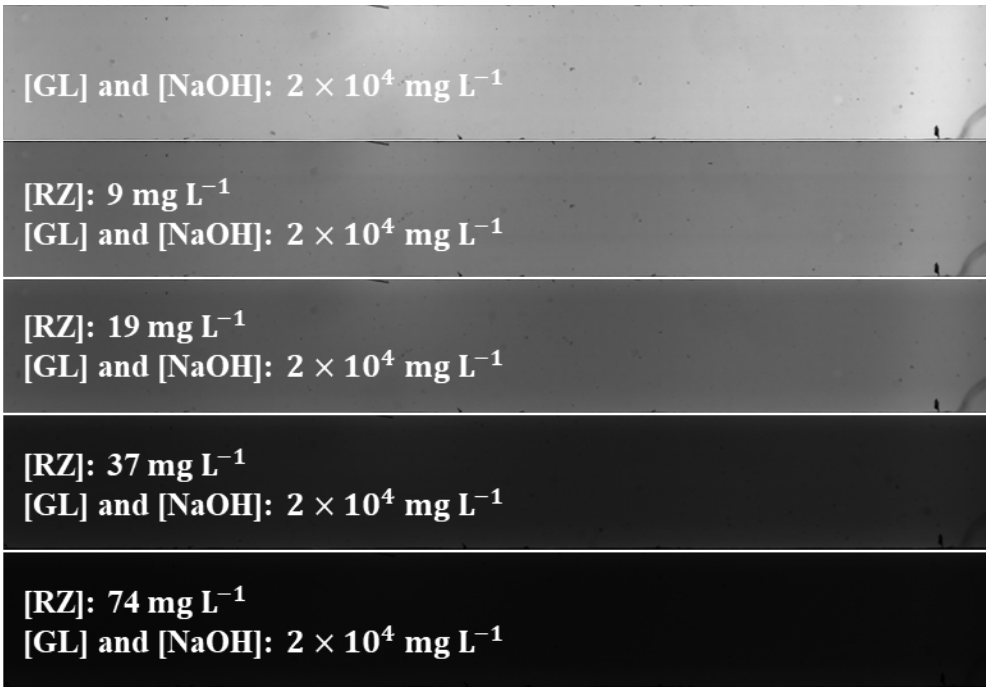

(a)

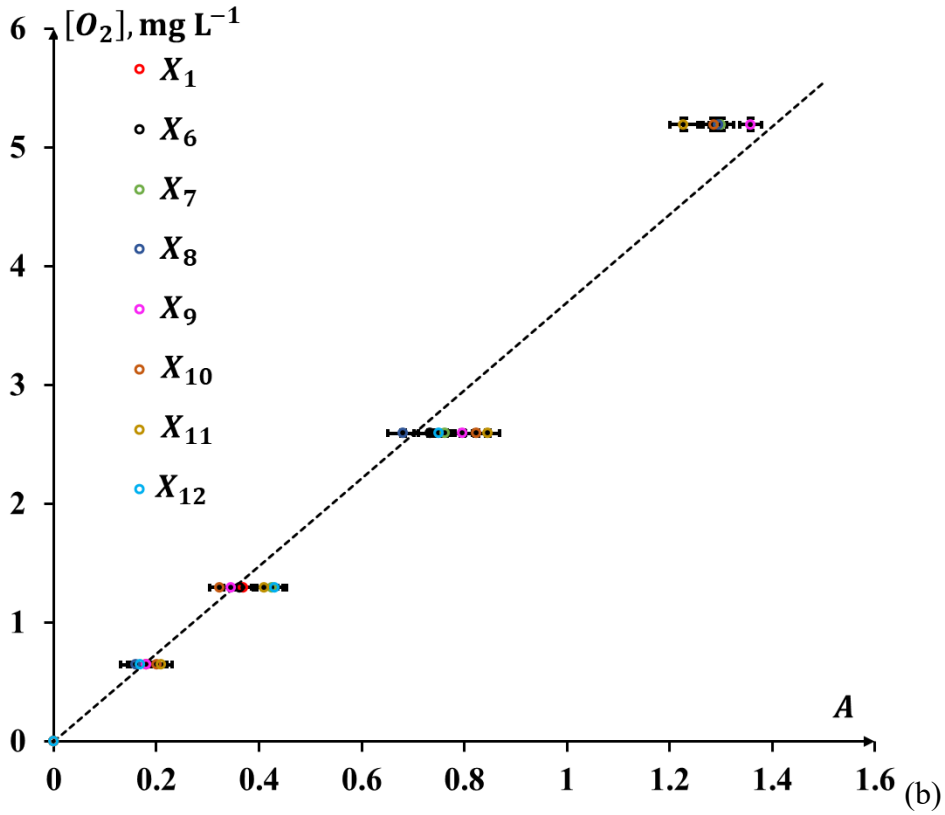

(b)

Fig. 2 Calibration process for mass transfer measurements (a) raw images of the millimetric channel containing solutions at different resorufin concentrations [RF]. (b) Calibration relationship between equivalent O_2 concentration and the absorbance of resorufin (RF) at different axial positions (the dotted line represents the fitted linear relationship between the RF concentration and the absorbance).

The absorbance, A, could be deduced from the time-averaged gray level values as follows:

$$A = -\log\left(\frac{\bar{I}}{\bar{I}_0}\right) \quad (2)$$

where $\bar{I}_0$ and $\bar{I}$ were the averaged gray intensities when no dye was present in the solution ([RF]=0) and at a given RF concentration respectively. They were obtained considering all the pixels inside of channels and for a given ROI position.

Note that, contrary to the study presented in Mei et al. (2020b), a "global" calibration (instead of a pixel-by-pixel calibration) was implemented here as there was no radial change of the light penetration depth in the present case (the setup involved a square channel and not a tube). Furthermore, a Beer-Lambert law type relationship linking the absorbance to the resorufin concentration [RF] could be applied (instead of a linear one, as in Mei et al. (2020b)) because the light was monochromatic (green LED and NE2R10A absorptive ND filter was used, see Part I).

Knowing [RF], the equivalent O_2 concentration into the global window of observation was deduced considering the stoichiometry of the reaction (i.e., one mole of DH reacted with 0.5 moles of oxygen to form one mole of RF).

Finally, as shown in Fig. 2 (b), whatever the observing position X_i, the following calibration relationship between the equivalent O_2 concentration and the absorbance of RF was obtained (corresponding to the dotted line in Fig. 2 (b)):

$$[O_2] = 3.70 \times A \quad (3)$$

with a mean absolute percentage error of regression (MAPER, see the Supplementary Material S1) equal to 11%.

For reminder, the term “equivalent” was used because in reality the oxygen concentration in the liquid phase was null: indeed, oxygen was fully consumed by DH to form RF, according to an instantaneous oxidation reaction (see Yang et al. (2016b)).

In Fig. 2(b), some slight differences could be observed between the different ROI positions: they were probably caused by the uncertainty of each calibration and the variations of light at different positions.

Fig. 3 presents the main steps of the image processing, starting from a raw image of gas-liquid flow. It consisted of four steps for the image processing:

(i) Identifying liquid slugs and bubbles from the images and removing bubbles from the images, as shown in Fig. 3 (b) and (c).

(ii) Converting gray level values in the liquid slugs into the absorbances using Eq. (2).

(iii) Obtaining equivalent O_2 concentrations using the established calibration relationship in Fig. 2 (c).

(iv) Plotting the equivalent O_2 concentration fields shown in Fig. 3 (d).

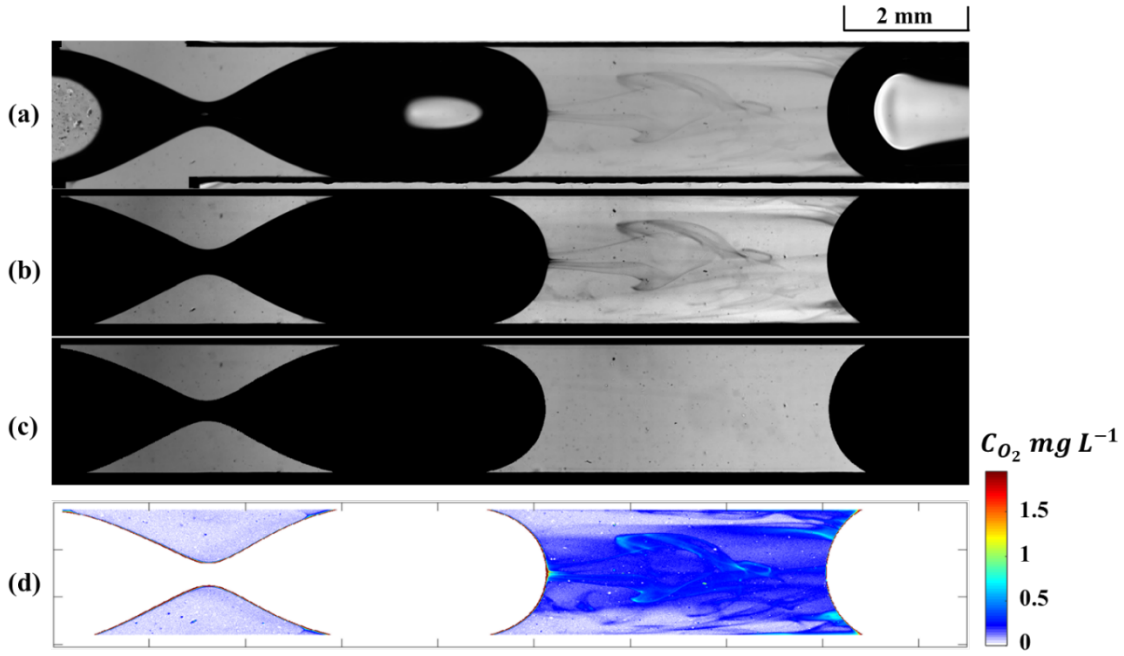

Fig. 3 Main steps of the image processing: (a) Raw image of gas-liquid flow. (b) Image with remaining liquid of RF signal. (c) Background image of remaining liquid without RF signal. (d) Equivalent O_2 concentration field in the liquid slug. Operating condition: j_L = 17.9 cm· s^{-1}, j_{G0} = 10.7 cm· s^{-1}.

As a reminder, the gray level intensity, *I*, recorded for each pixel was an overall value resulting from the contributions of different *x*-*y* planes along the depth direction (i.e., *z* direction). It is important to recall that, from a theoretical point of view, these gray level intensity values could not be linearly added together (because of the exponential attenuation of light), whereas the absorbance values could be. Therefore, for each pixel, the obtained absorbance corresponded to the summation of the absorbances at different *x*-*y* planes along the depth direction. In addition, it should be kept in mind that the Beer-Lambert law should be applied at given wavelength only if the concentration of the absorbing specie (here RZ) is homogeneous in the depth direction. In the present experiments, due to the 3D flow structure in the liquid slug,

some gradients of oxygen concentration inevitably existed in the depth direction. Unfortunately, this level of heterogeneities could not be captured by the method, and all the more that it depended on the operating conditions. The heterogeneity was here defined as a percentage of the standard deviation errors (SD, see Supplementary Material S1) with respect to the averaged equivalent oxygen concentrations inside of the liquid slug. Taking five representative operating conditions under j_{TP} = 28.6 cm· s^{-1}, and twelve ROI observing positions, the heterogeneities were estimated between 1% and 20% and decreased with the ROI observing positions.

3. Results and discussion

3.1 Equivalent O2 concentration fields

By implementing the colorimetric technique and applying the image processing, the equivalent O_2 concentration fields in the liquid slugs could be obtained at the cross-junction and after, at different axial positions in the channel.

The critical Capillary number for the transition between a circular cross-sectional shape of the bubble and a square one with curved corners occurred at 10^{-2} according to Boden et al. (2014) and Fries et al. (2008). As the two-phase Ca number were below 8.5×10^{-3} in this study (see Part I), the liquid film thickness between bubble and channel side walls, δ_{wall}, could be considered as constant according to Fries et al. (2008), and close to 2% of the hydraulic diameter of the channel (i.e., $\delta_{wall} \approx 43\ \mu m$). The spatial resolution of the images was at 8.25 μm per pixel, meaning that the liquid film could be visualized by around 5 pixels theoretically. However, it was not possible

to experimentally measure the gray level variation between the bubble and channel wall. Therefore, in this study, the concentration fields in the liquid film close to the wall could not be measured.

3.1.1 During the bubble formation process

The time-variation of equivalent O_2 concentration fields during the bubble pinch-off process is described in Fig. 4 for various operating conditions.

Fig. 4 (a) presents a case where the pinch-off process covered an extremely long period of 3975 ms (around half of the whole pinch-off process). Under this condition, the associated Ca_{TP} and Re_{TP} were equal to 5.9×10^{-5} and 8, respectively. The capillary force was thus dominant compared to the viscous and inertial forces. Before the pinch-off point (-112.5 ms < t < -2.5 ms), some layers of dissolved O_2 formed on both sides of the gas finger neck and became gradually thicker. At the bubble pinch-off point, these layers merged, generating a jet-like central oxygen concentration 'finger' between the just-formed bubble and the gas finger. Then the gas finger grew, protruded into the main channel, and finally blocked the main channel (0 < t < 2112.5 ms). During this stage, the dissolved O_2 was transported by the entering liquid from inlets. As the Reynolds number was very low, the equivalent O_2 field remained highly symmetric with respect to the centerline of the main channel. Once the main channel was fully blocked by the coming gas finger (2612.5 < t < 3862.5 ms), the liquid from the inlets hardly entered into the main channel and the recirculation loop started to develop inside the liquid slug. Therefore, as the liquid flow inside the liquid slug presented higher velocities along the centerline and a negative velocity near the channel wall, the dissolved O_2 concentration was transported from the tip of the gas finger to the rear of the formed bubble. In the

meantime, the thickness of the dissolved O_2 region near gas finger got thicker, enabling to better disperse oxygen in the radial direction of channel.

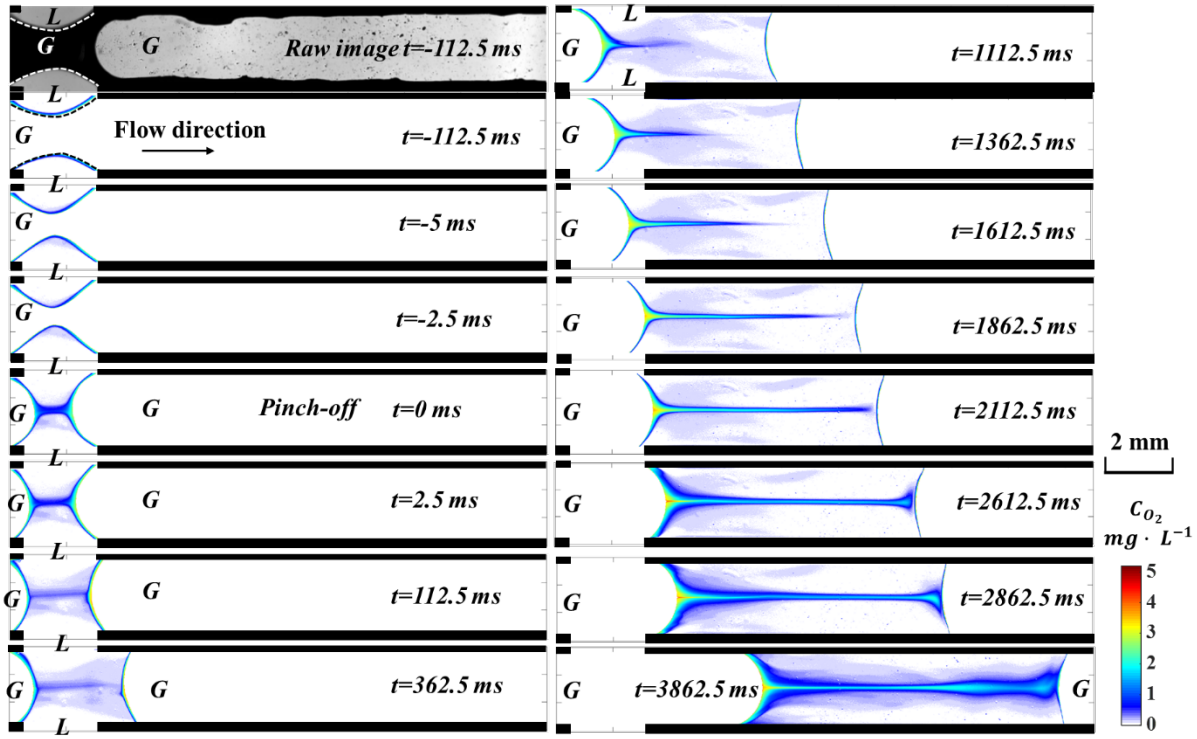

(a)

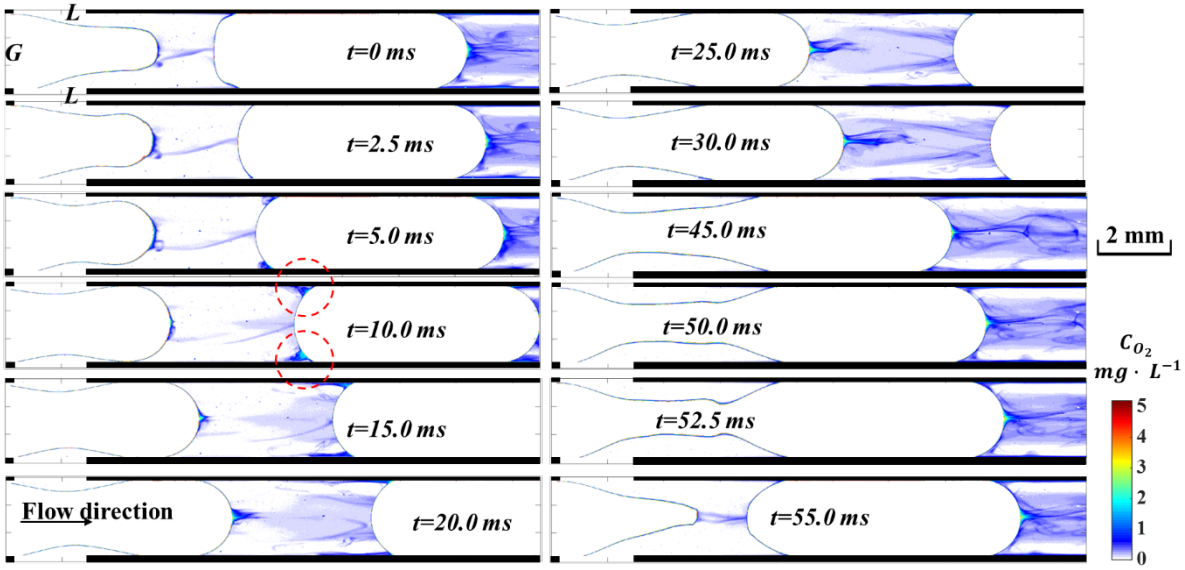

(b)

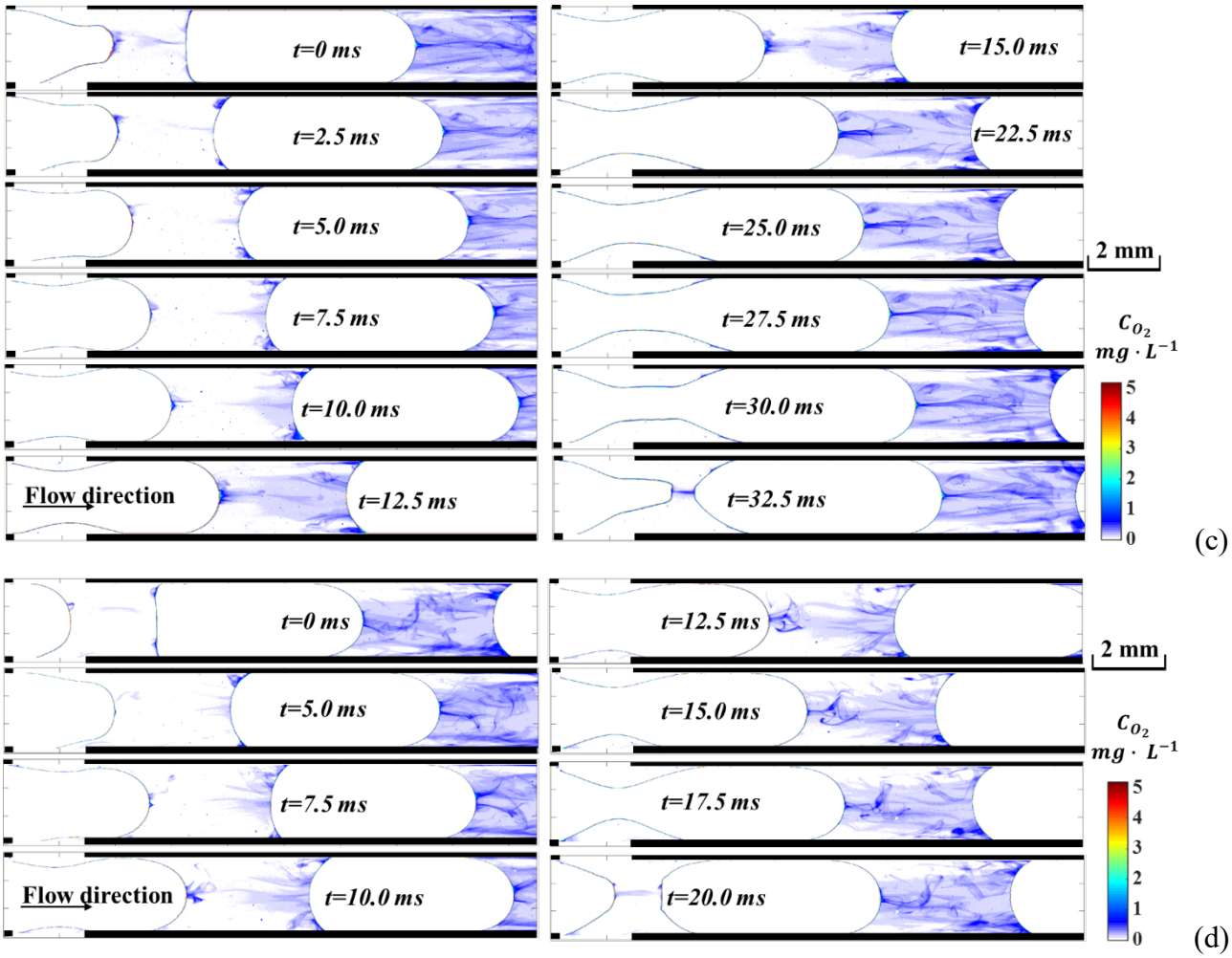

Fig. 4 Time-variation of the equivalent O_2 concentration fields during the bubble pinch-off process for various operating conditions at $X_1 = 0$ mm: (a) $j_L = 0.2$, $j_{G0} = 0.2$ cm· s^{-1} and $Re_{TP} = 8$, (b) $j_L = 10.7$, $j_{G0} = 10.7$ cm· s^{-1} and $Re_{TP} = 416$, (c) $j_L = 14.3$, $j_{G0} = 14.3$ cm· s^{-1} and $Re_{TP} = 555$, (d) $j_L = 21.4$, $j_{G0} = 21.4$ cm· s^{-1} and $Re_{TP} = 832$.

Fig. 4 also shows the time-variation of the equivalent O_2 concentration fields for three other operating conditions, where the gas-liquid superficial velocity ratio η_0 was equal to 1 and the corresponding Ca_{TP} and We_{TP} to 3.2×10^{-3} and 1.3 (case (b)), 4.3×10^{-3} and 2.7 (case (c)), 6.4×10^{-3} and 5.3 (case (d)). In these cases, the whole bubble formation period was shortened due to higher gas and liquid superficial velocities (55 ms, 32.5 ms and 20 ms respectively, against 8247.5 ms in the case (a)). One can observe

that the jet-like central oxygen concentration 'finger' at the centerline became no more visible from Fig. 4 (b) to (d), as the times to break up the gas finger were shortened (up to 412 times lower compared to case (a)). Furthermore, when increasing two-phase Reynolds number Re_{TP}, the recirculation loop developed faster in the liquid slug. Contrary to Fig. 4 (a), at the stage where the main channel was fully blocked by the coming gas finger, two spots of high equivalent O_2 concentration could be distinguished near the formed bubble rear and channel wall region, marked by two red circles in Fig. 4 (b). This phenomenon could be attributed to the developed recirculating loop inside of liquid slug. Indeed, in the region between the bubble rear and the channel wall, the liquid flow came from the centerline and turned backwards along the channel wall, thus carrying the dissolved oxygen due to the diffusive transport between the liquid and the bubble rear (Abiev, 2020). It was also possible that the liquid coming from the channel corner (surrounding the front bubble) could contribute to these two spots of high equivalent O_2 concentration, because of the diffusive transport between the liquid film in the corner and the bubble lateral body, and the convective transport within the liquid film (Abiev, 2020).

3.1.2 During the bubble flowing process

In Fig. 5, the equivalent O_2 concentration fields are plotted for different flowing times at a total two-phase superficial velocity j_{TP} of 28.6 cm s^{-1} and for different gas-liquid superficial velocity ratio η_0. The flowing time was calculated by dividing the observing position X_i by the bubble velocity U_B, and thus corresponded to the time required for the liquid slug to travel to the axial position X_i. The related Ca_{TP} and We_{TP} numbers were equal to 4.3×10^{-3} and 2.4, respectively. Therefore, the effects of η_0 on the

equivalent O_2 concentration fields could be quantified by comparing Fig. 5 (a), (b) and (c). One can observe that the oxygen dissolved inside the liquid slug became higher as far as the bubbles flowed inside the channel (i.e., with increasing axial positions or flowing times). At X_2 = 17 mm, where the liquid slug was not far from the bubble formation point, the recirculating flow inside of liquid slug was not yet fully formed. Along the centerline region and near wall region of the liquid slug, the equivalent O_2 concentration presented higher values than the ones of other regions, due to the convective transport of oxygen by the recirculation loop and within the liquid film (Abiev, 2020). However, in some cases, the region near the bubble rear along the centerline also presented a lower equivalent O_2 concentration, which may be induced by the complex 3D flow structure (combined effects of the horizontal and vertical flow structures). As the bubble flowed along the channel, the tip region near the bubble nose always held higher equivalent O_2 concentrations until reaching an almost uniform field, as seen in the last position X_{12} in Fig. 5 (a). However, in Fig. 5 (b) and (c), even for the last position X_{12}, some gradients of equivalent O_2 concentration still existed inside the liquid slug. Therefore, at an identical two-phase superficial velocity j_{TP} (i.e., at almost same bubble velocity), an increase of gas-liquid superficial velocity ratios η_0 (i.e., shorter liquid slugs) led to improve the mixing inside the liquid slug, to increase the equivalent O_2 concentration and further to enhance the mass transfer from gas phase to liquid phase.

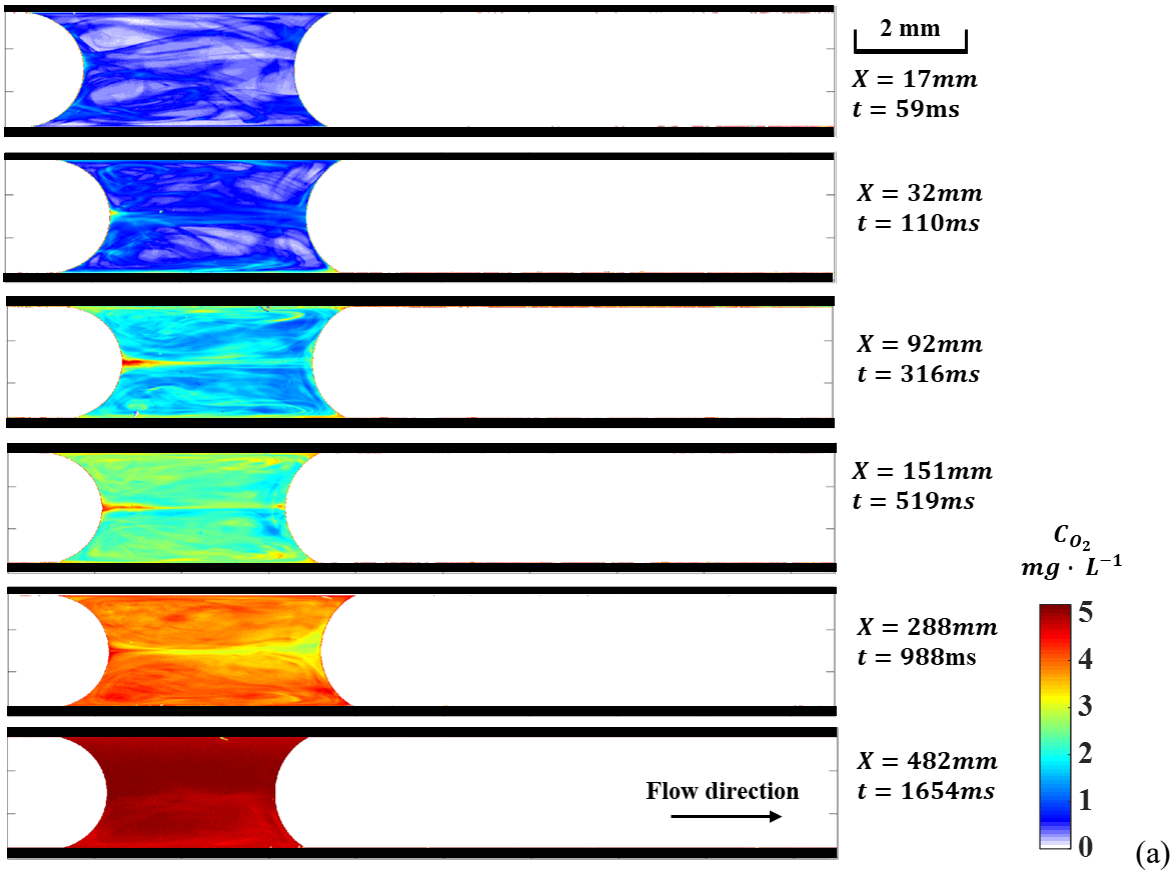
2 mm
X = 17mm
t = 59ms
X = 32mm
t = 110ms
X = 92mm
t = 316ms
X = 151mm
t = 519ms
X = 288mm
t = 988ms
X = 482mm
t = 1654ms
Flow direction
C_O2
mg · L^-1
5
4
3
2
1
0

(a)

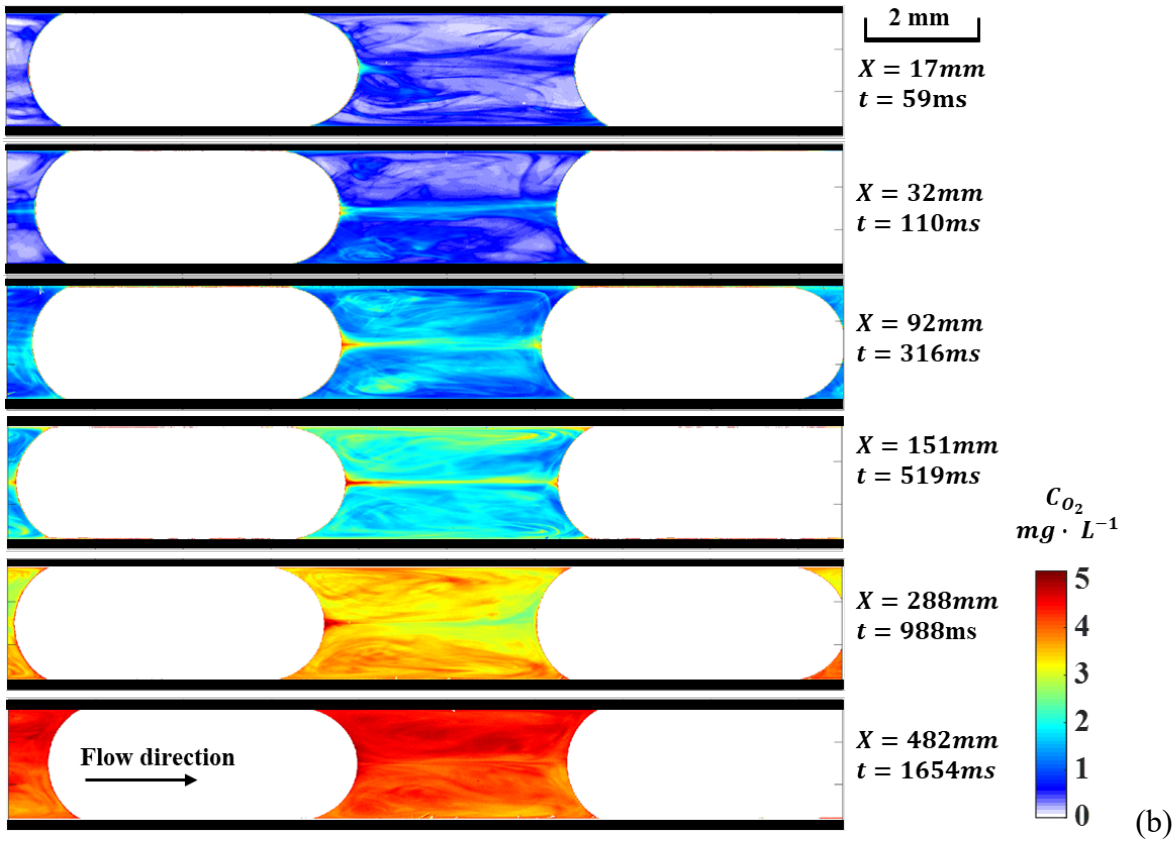
2 mm
X = 17mm
t = 59ms
X = 32mm
t = 110ms
X = 92mm
t = 316ms
X = 151mm
t = 519ms
X = 288mm
t = 988ms
X = 482mm
t = 1654ms
Flow direction
C_O2
mg · L^-1
5
4
3
2
1
0

(b)

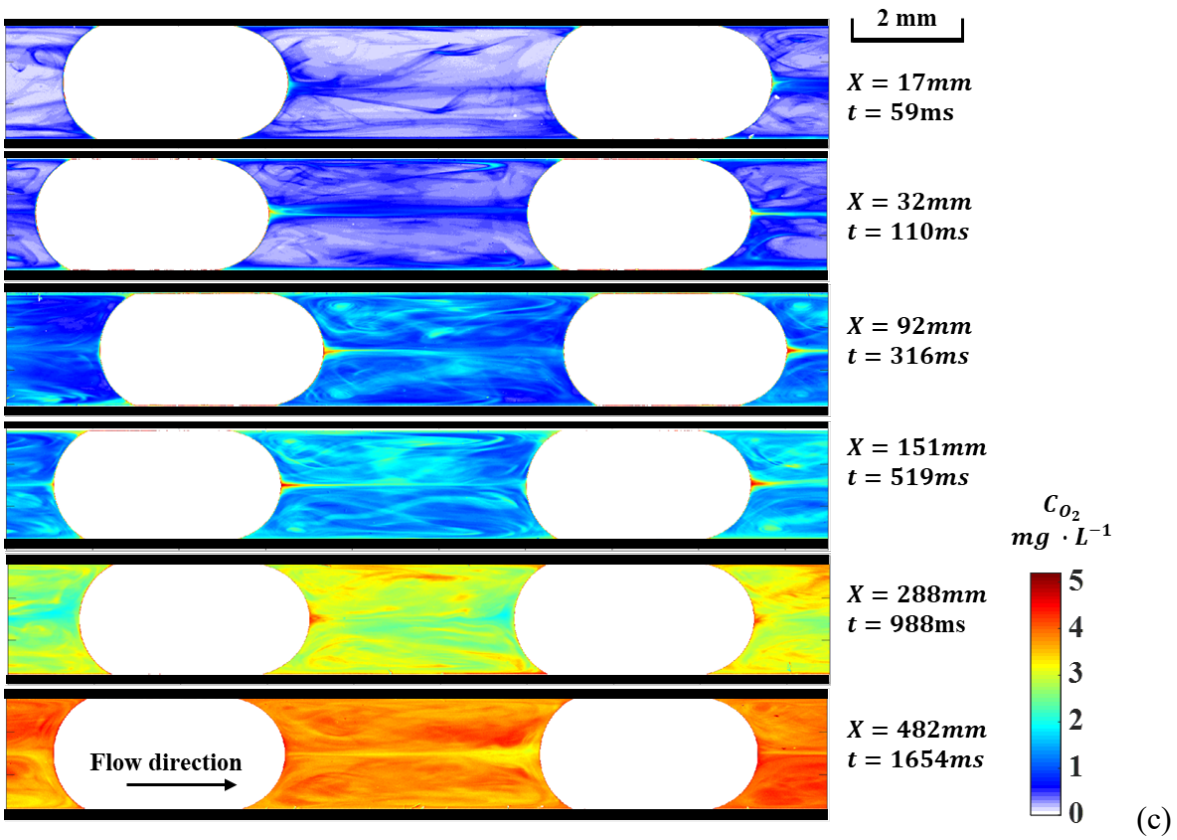

Fig. 5 Equivalent O_2 concentration fields during the bubble flowing process at j_{TP} = 28.6 cm· s^{-1} under different gas-liquid superficial velocity ratio: (a) η_0 = 3.0, (b) η_0 = 1.0, (c) η_0 = 0.6. Black arrows indicate the flow direction.

3.2 Axial variation of the concentration and mass flux density

The averaged O_2 concentrations could be calculated at different observing positions X_i, as follows:

$$\overline{C_{O_2}}(X) = \frac{\iiint C(x,y)\cdot dx\cdot dy\cdot dz}{L_s\cdot {d_h}^2}, \tag{4}$$

where $\overline{C_{O_2}}(X)$ was the equivalent oxygen concentration at an axial location X_i as depicted in Fig. 5 and measured only in the liquid slug, Ls the slug length and d_h the hydraulic diameter of the channel (see Part I).

Fig. 6 plots this averaged concentration, $\overline{C_{O_2}}$, normalized by the maximum oxygen concentration C_{max} (i.e., 5.2 mg· L^{-1}, see section 2.2) as a function of the axial positions, for each two-phase superficial velocity j_{TP} and for different gas-liquid superficial velocity ratio, η_0 (other conditions are plotted in the Supplementary Material S2). At a given j_{TP}, an increase of gas-liquid superficial velocity ratio η_0 logically increased the amount of oxygen transferred by unit of liquid slug volume, as observed in Fig. 5. When $\overline{C_{O_2}}/C_{max}$ kept below 0.8, the normalized O_2 concentrations increased linearly with axial positions.

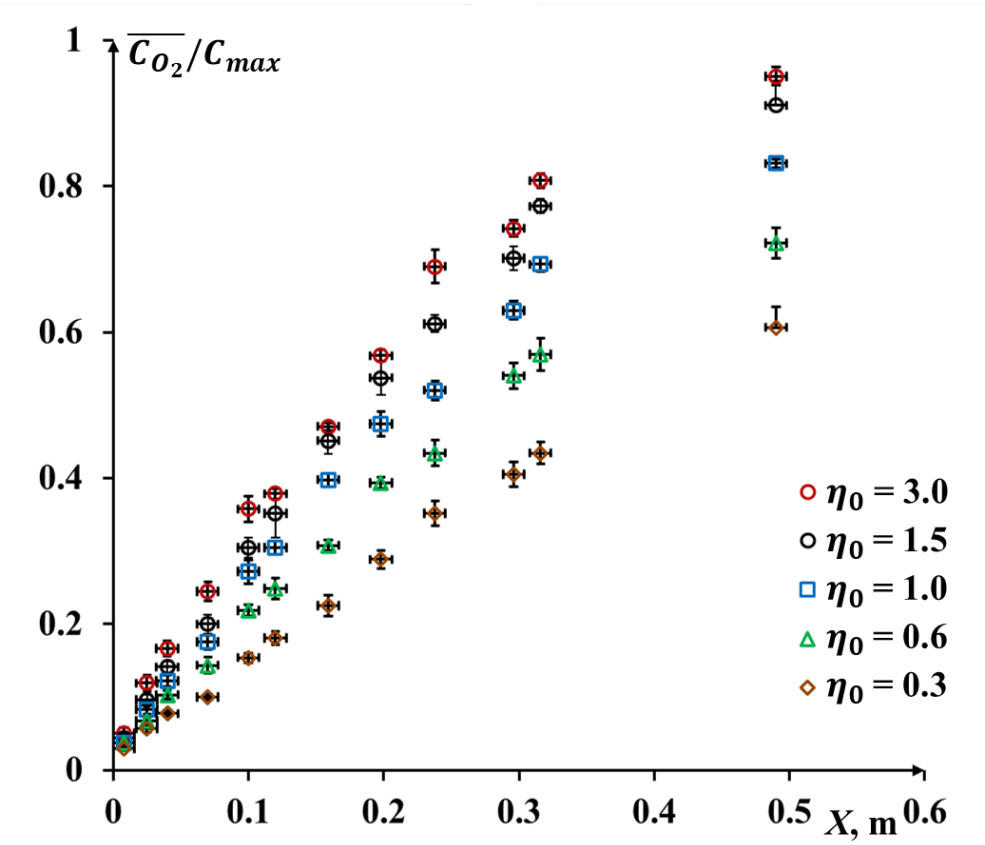

Fig. 6 Axial variation of normalized averaged equivalent O_2 concentrations in the liquid slug for different operating conditions: j_{TP} = 28.6 cm· s^{-1} and Re_{TP} = 555.

In addition, the mass flux density cumulated in the liquid slugs along the axial positions, noted φ_{O_2}, was calculated according to the equation defined in Mei et al. (2020b):

$$\varphi_{O_2}(X) = \frac{U_B}{S_B}\frac{\mathrm{d}m_{O_2}(X)}{dX} \quad (5)$$

where the bubble velocity U_B and bubble surface S_B were obtained in the Part I of the article. These parameters were considered constant along the channel length (the bubble nose and rear were assumed as hemispherical shape, see Supplementary Material S3).

As shown in Fig. 7, whatever j_{TP} and η_0, the mass flux density, φ_{O_2}, sharply decreased over the first millimeters after the cross-junction and finally tended towards a plateau. At given axial position X and j_{TP}, an increase of η_0 induced higher mass flux densities, and at given axial position X and η_0, an increase of j_{TP} also induced higher mass flux densities. One can note that, for all operating conditions, the mass flux densities became constant after 0.2 m. After this location from the cross-junction (almost 10 times the hydraulic diameter of the channel), the entrance effects (bubble formation stage) had no more influence. Note that the same trends were observed for other values of j_{TP} (see Supplementary Material S4).

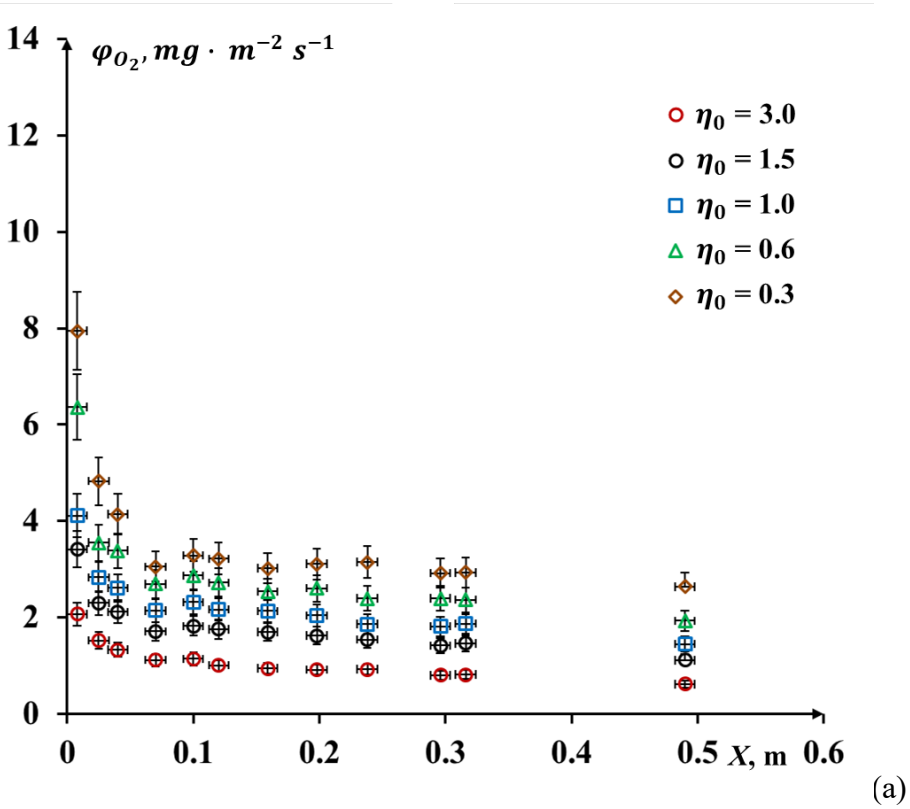

(a)

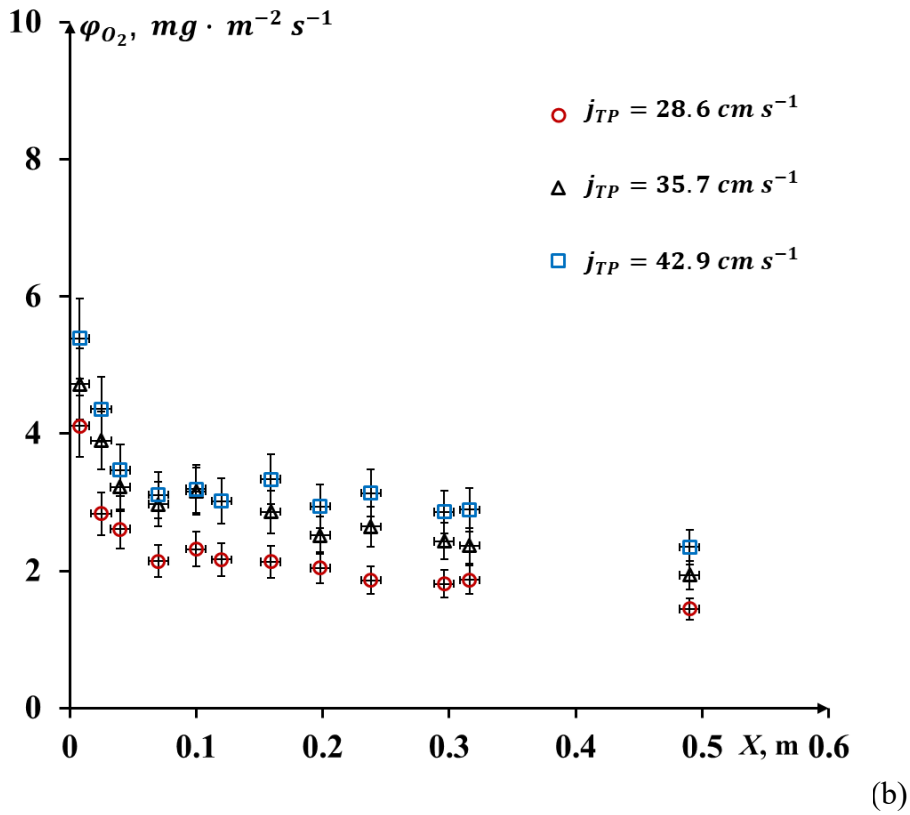

(b)

Fig. 7 Variation of the mass flux density with the axial positions under different operating conditions: (a) j_{TP} = 28.6 cm· s^{-1}; (b) η_0 = 1.0.

3.3 Estimation of enhancement factor

Due to the chemical reaction between oxygen and dihydroresorufin, the chemical enhancement factor E (the ratio between the average mass fluxes with the resazurin-based reaction) should be estimated. The Hatta number Ha (the ratio between the reaction rate and the diffusion rate in the liquid film) and E could be calculated by solving two implicit equations, as presented in Mei et al. (2020b) (the related equations are given in the Supplementary Material S5). In the present study, the oxygen concentration at saturation ($C_{O_2}^*$) was considered equal to 8.15 mg L^{-1} (no bubble expansion, pressure drop below 7 kPa).

The related reaction rate constants k_2 was initially considered equal to 1.28×10^6 $L\cdot mol^{-1}$ s^{-1} (Yang et al. (2016b)), and later to 0.67×10^6 $L\cdot mol^{-1}$ s^{-1} (Hoppe (2019)). For all the conditions displayed in Fig. 7, whatever the value of k_2 considered,

- when the Hatta numbers ranged between 3 and 8.6, the enhancement factors were between 1.02 and 1.04.
- when Ha ranged from 0.65 to 3, E tended towards to unity.

Thus, these calculations would suggest that the enhancement caused by the colorimetric chemical reaction on the mass transfer could be assumed negligible. Thus, E was considered as unity in the following section.

3.4 Cumulated oxygen mass during bubble formation process

This sub-section aims at analyzing the oxygen mass that was cumulated inside one liquid slug during the formation of the Taylor bubble. For that, the considered liquid slug was the one in front of the forming bubble.

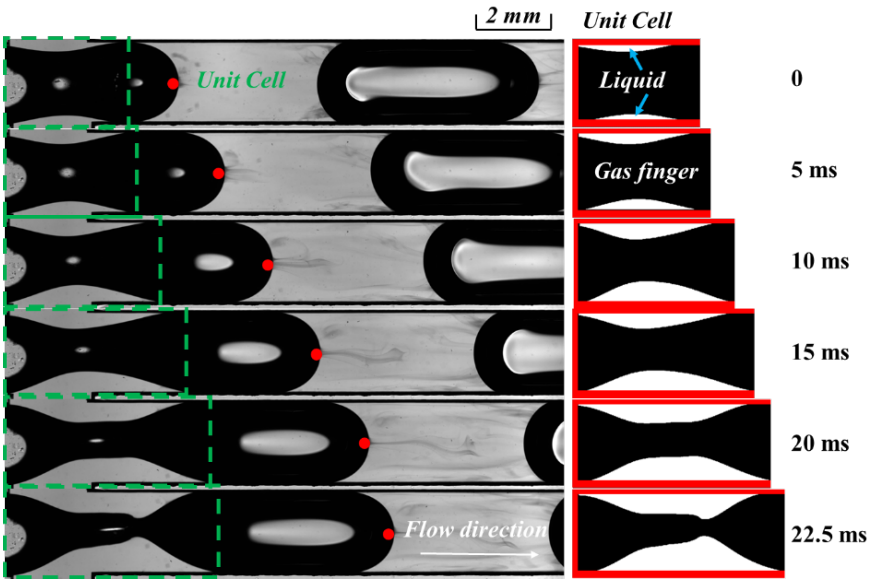

(a)

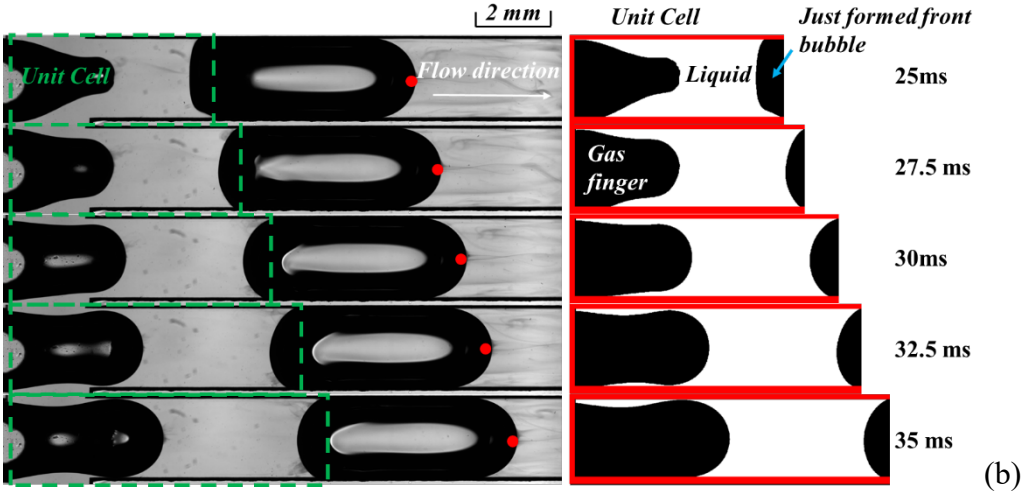

(b)

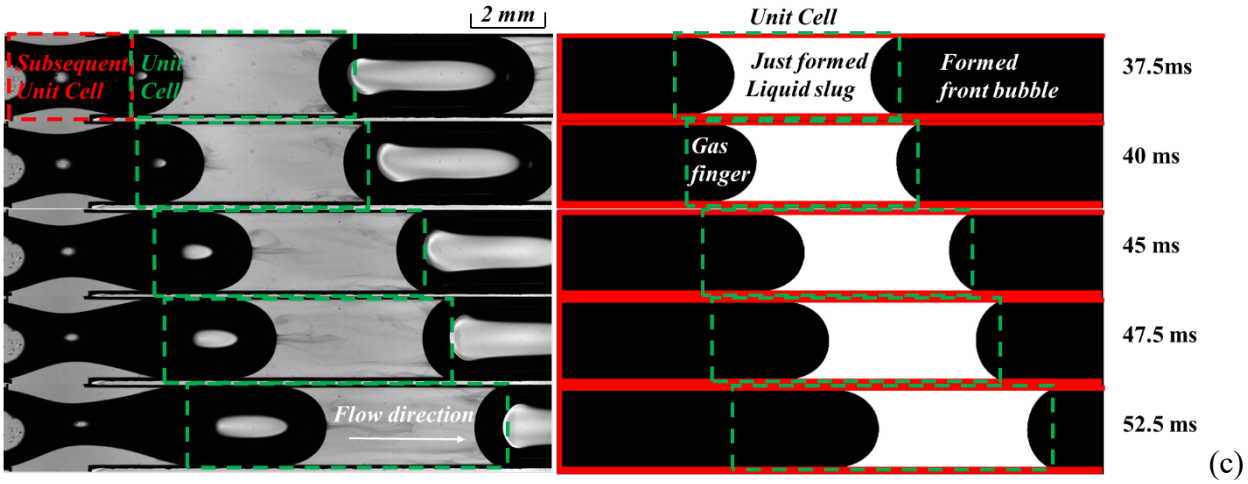

Fig. 8 Illustration of the development of unit cell, liquid slug and bubble during the bubble formation process. Stage (a) corresponds to the squeezing liquid surrounding the gas finger, stage (b) to the entering liquid after the pinch-off of the front bubble but before the block of channel by gas finger, and stage (c) to the liquid slug separated by gas finger and formed bubble. Operating conditions: η_0 = 1.0, j_{TP} = 28.6 cm· s^{-1}, Ca_{TP} = 4.3×10^{-3}, We_{TP} = 2.4.

Fig. 8 presents some image sequences relating to the development of the liquid slug. They show that the liquid slug could be divided into three stages:

a. the liquid surrounding the gas finger neck, squeezed the gas finger until the pinch-off of the front bubble.

b. after the pinch-off of the front bubble, the liquid entered the main channel until the back gas finger fully blocked the channel.

c. the liquid slug formed and was separated by the back gas finger and front formed bubble.

Note that, in Fig. 8, the images on the right column correspond to the zones occupied by the liquid phase that were extracted using Matlab® software. The unit cell was here marked by the green dotted box.

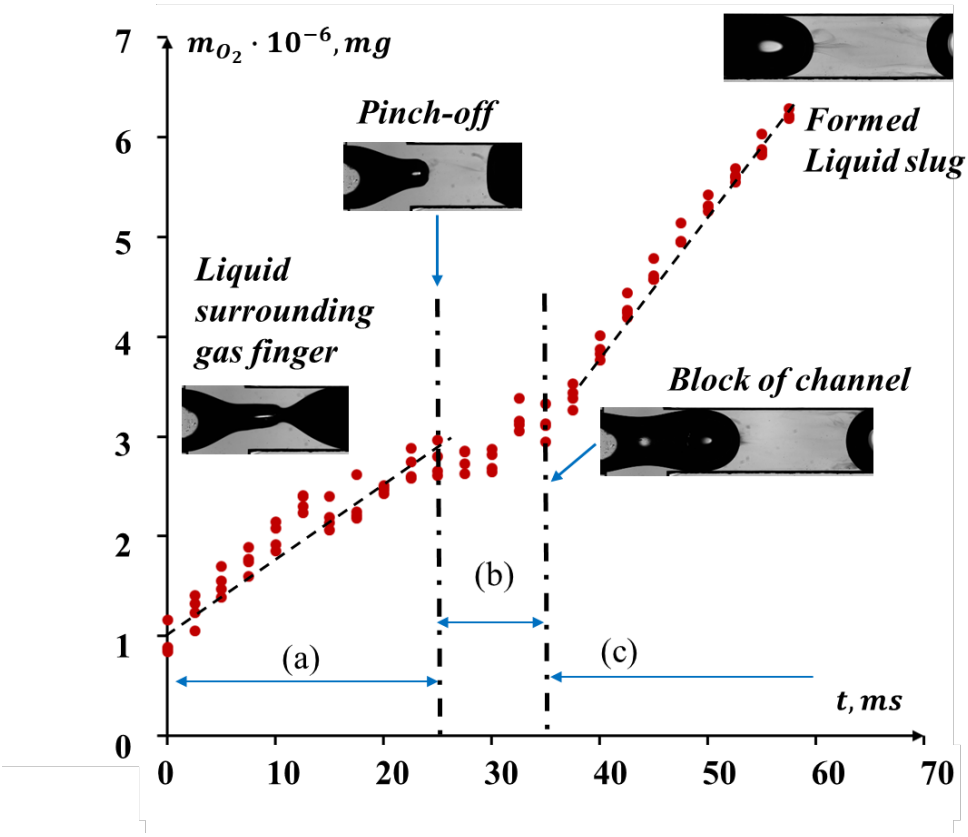

Fig. 9 Evolution of cumulated oxygen mass inside the liquid phase during bubble formation pinch-off process for three stages (a), (b) and (c). Operating conditions: η_0 = 1.0, j_{TP} = 28.6 cm· s^{-1}, Ca = 4.3×10^{-3}, We = 2.4.

Fig. 9 displays a typical variation of the oxygen mass cumulated in the liquid during the bubble formation. The same three stages than in Fig. 8 could be distinguished. During the stages (a) and (c), the cumulated oxygen mass increased almost linearly with time. The gas finger velocity in stage (a) and the formed bubble velocity in stage (b) were estimated according to the displacement of the gas finger nose or bubble nose (see solid red dots in Fig. 8). They showed that, during the stage (a), the gas finger was accelerating until the bubble pinch-off with velocities ranged from 24.8 to 28.1 cm· s^{-1}, while during the stage (b), the formed bubble velocity was almost constant around 28.6 cm· s^{-1}. The fast rate of oxygen mass in stage (c) could be thus due to the consequences

of the developing recirculation loop in the formed liquid slug and also of the accelerating movement of subsequent gas finger. During the stage (b), the oxygen mass slightly varied, probably due to a 'dilution effect' induced by the fresh liquid coming from side channels.

In the future, deeper studies relating the local variations of mass transfer rates and the gas finger velocities need to be further implemented to have a better understanding.

3.5 Overall mass transfer coefficients

The overall volumetric liquid side mass transfer coefficient, $k_L{\cdot}a$, could be deduced from the oxygen mass balance in the liquid phase according to Eq. (6).

$$\frac{\mathrm{d}\overline{C_{O_2}(X)}}{\mathrm{d}t} = E\ k_L(X)\ a(X)\ (C^*_{O_2}(X) - \overline{C_{O_2}(X)_{rl}}) \quad (6)$$

where t represented the flowing time of the bubble until reaching the axial position ($t = X/U_B$) and $\overline{C_{O_2}(X)_{rl}}$ was equal to zero because of a full consumption of O_2 by DH in the liquid slug. The enhancement factor E was considered equal to 1 (see section 3.3).

From the axial variations of equivalent O_2 concentration (Fig. 6), $\overline{C_{O_2}(X)}$ could be considered as linearly increasing with X (i.e., time t). Using the least square method, the slope coefficient (noted ζ) between $\overline{C_{O_2}(X)}$ and X could be obtained considering a linear relation when $\overline{C_{O_2}}/C_{max}$ was below 0.8. Therefore, the overall volumetric liquid side mass transfer coefficient $k_L{\cdot}a$ could be directly deduced from

$$k_{\mathrm{L}}\, a = \frac{\zeta \times U_B}{C^*_{\mathrm{O_2}}} \tag{7}$$

As the mass transfer mechanism was mainly affected by the recirculation loops inside the liquid slug, it was interesting to compare these coefficients with the frequencies of loop recirculation, f_c, defined by Abiev et al. (2019) as

$$f_c \approx \frac{U_B}{4L_S} \tag{8}$$

The numerical values of the overall volumetric liquid side mass transfer coefficients $k_L \cdot a$ and the recirculation frequencies f_c are reported in the Supplementary Material S6.

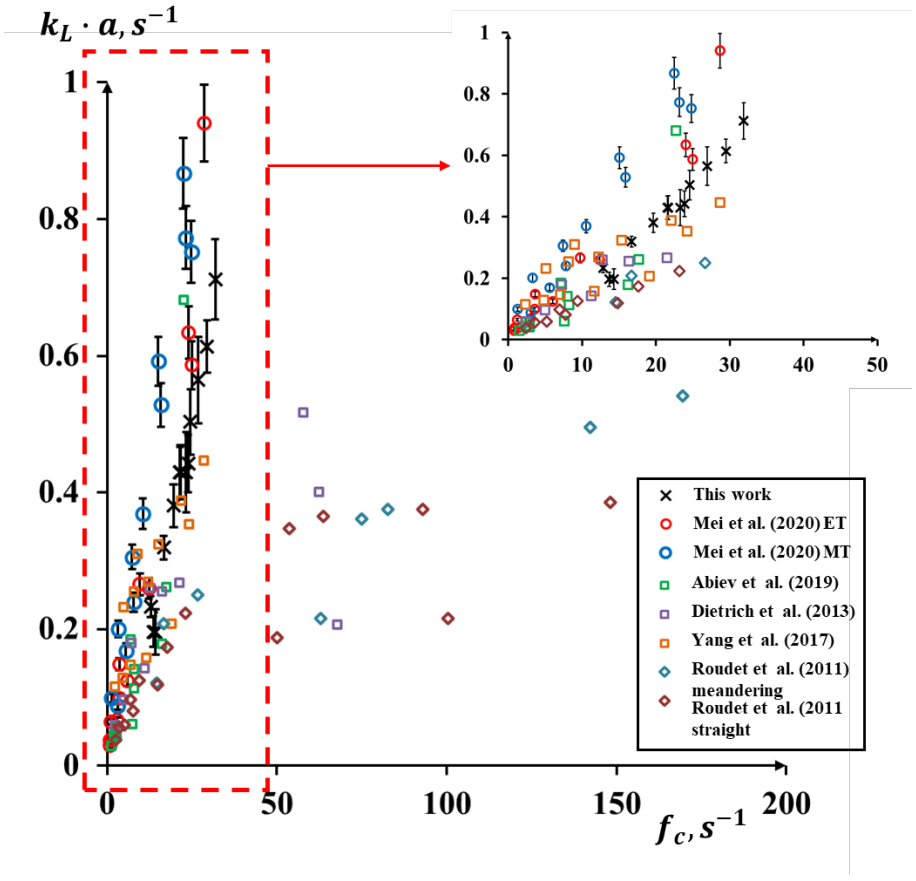

Fig. 10 Relationships between the overall volumetric liquid-side mass transfer coefficients $k_L\, a$ and

the recirculation frequencies, f_c, for the three different configurations investigated in this work and for the data from the literature.

Fig. 10 plots the overall volumetric liquid side mass transfer coefficient, $k_L \cdot a$, as a function of the recirculation frequency, f_c , obtained in the present work (i.e., in the straight milli-channel with a cross-junction), as well as the ones measured by Mei et al. (2020b) in different in-plane spiral-shaped tubes. Whatever the cases, $k_L \cdot a$ followed a linear increase relation with f_c, that could be described by the following correlation proposed by (Mei et al., 2020b):

$$k_L \cdot a = \omega f_c \tag{9}$$

The coefficient ω was found equal to 1.99×10^{-2} in the present straight channel. This coefficient was lower than the ones obtained in the in-plane spiral-shaped milli-reactor (2.75×10^{-2} and 3.45×10^{-2}, Mei et al. (2020b)), which was possibly due to the absence of centrifugal force, different cross-sectional shapes (cylindrical tube versus squared channel), and channel dimensions. In addition, the minimal Re_{TP} number in the present study was about 2.4 times of the maximal Re_{TP} number in the spiral-shaped reactor. This emphasized the mass transfer intensification caused by the centrifugal force even under lower ranges of Re_{TP} number.

In addition, the data of Roudet et al. (2011) in straight and meandering channels (2mm, square), Yang et al. (2017) in a meandering milli-channel (2mm, square), Dietrich et al. (2013) in a straight milli-channel (2mm, square), and Abiev et al. (2019) in a vertical glass tube (d_{it}, 3mm), were plotted in Fig. 10. They also followed a good linearity when the recirculation frequencies were lower than 50. Above this value, the

overall volumetric liquid side mass transfer coefficient $k_L \cdot a$ remained almost constant, which was probably due to other factors (e.g., possibilities of bypass flow, shorter flowing time inside of the milli-channels).

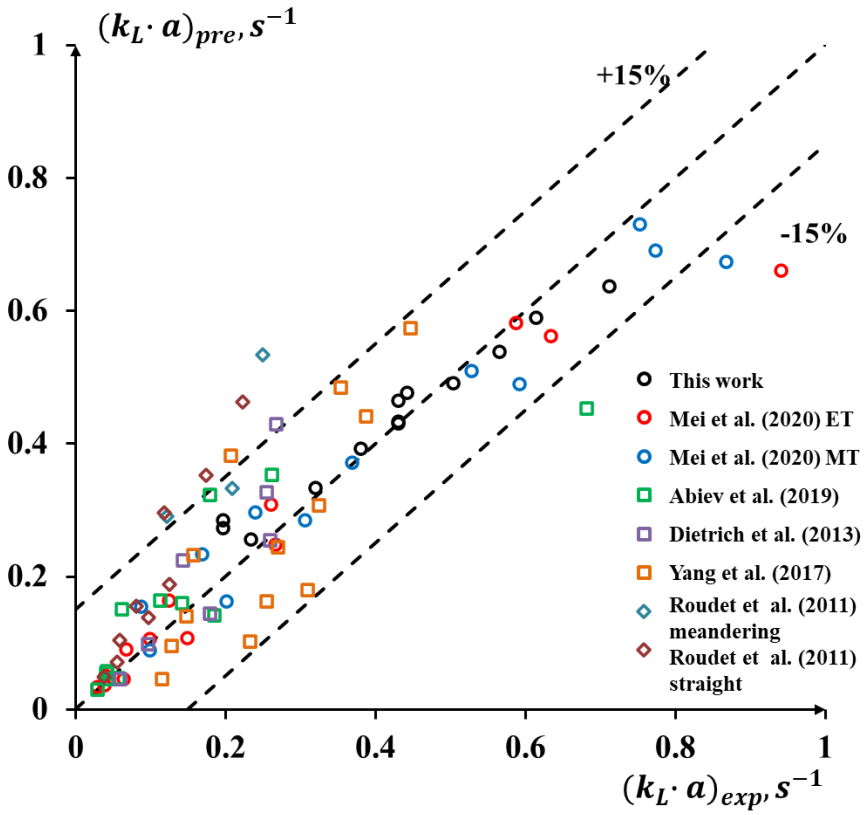

Fig. 11 Comparison between the predicted $(k_L\ a)_{pre}$ and experimental $(k_L\ a)_{exp}$ for the configuration investigated in this work and for the data from the literature.

As explained by Mei et al. (2020b), the intensification factor for $k_L \cdot a$ was almost proportional to the increase of $\sqrt{1/\langle\lambda\rangle}$ ($\lambda=2r/d_{it}$). For straight channels, the curvature ratio was infinity and $\sqrt{1/\langle\lambda\rangle}$ was thus zero. A scaling law for $k_L \cdot a$ considering f_c and $1/\langle\lambda\rangle$ was thus proposed to gather all the points for $f_c < 50$, which consisted of two terms as below:

$$\frac{k_L\, a}{f_c} = 2 \times 10^{-2} + \frac{270.10}{{f_c}^{0.56}} \left(\frac{1}{\langle \lambda \rangle}\right)^{1.91}, \qquad \text{MAPER: } 15.0\% \tag{10}$$

The first term was a constant own to straight channels, and the second term accounted for the effects of centrifugal force induced by the channel curvature.

Fig. 11 compares the predicted $(k_L\ a)_{pre}$ with the experimental $(k_L\ a)_{exp}$ for the configuration used in this work and also for the data from Roudet et al. (2011), Dietrich et al. (2013), Yang et al. (2017), and Abiev et al. (2019). One can observe that the scaling law proposed in Eq. (10) led to an acceptable description of all the configurations when recirculation frequencies were under 50.

4. Conclusions

The present work aimed at investigating the gas-liquid mass transfer around Taylor bubbles during and after the bubble formation (twelve observing positions) in a straight milli-channel with a cross-junction inlet geometry. Using the resazurin-based colorimetric technique and by improving image acquisition system (monochromatic light and higher magnification), the equivalent oxygen concentration fields were accurately visualized and measured. The main findings were the following:

1) The resazurin-based colorimetric method was implemented using a monochromatic light in the image acquisition system for the first time, thus allowing to apply the Beer-Lambert law to calculate the equivalent oxygen concentrations. However, one should keep in mind that the application of the Beer-Lamber law assumed that the concentration of dissolved species was homogeneous in the vertical direction, which

was not systematically the case in the experiments. The induced error was estimated between 1% and 20%.

2) The equivalent oxygen concentration fields could be measured with high spatial and temporal resolution. During the bubble formation stage, it was possible to distinguish different mechanisms for the developing oxygen concentration fields which depended on Re_{TP}. During the bubble flowing stage, the progressive accumulation of the dissolved oxygen inside the liquid slug was quantified as a function of the axial positions.

3) The average oxygen concentrations in the liquid slug increased linearly with the axial position X, while the mass flux density decreased with X until a location of almost 0.2 m. Furthermore, at the same flowing time for liquid slugs, it was found that the averaged oxygen concentrations increased with the gas-liquid superficial velocity ratio at given two-phase superficial velocities, and vice versa.

4) During the bubble formation, the evolution of the cumulated oxygen mass was described by three stages corresponding to (a) the oxygen present in the liquid surrounding the gas finger neck, (b) the oxygen accumulated in the liquid after the pinch-off of the front bubble, (c) the oxygen cumulated in the liquid slug (separated by the front bubble and back gas finger). The rate of cumulated oxygen mass was found the highest for the third stage, which was probably due to the combined effect of the developing recirculation loop and of the accelerating gas finger.

5) The overall volumetric liquid side mass transfer coefficients ($k_L\,a$) obtained in the present work were compared with the ones measured in the literature. They followed a linear increase with the recirculation frequencies for $f_c < 50$. A scaling law

based on recirculation frequency and curvature ratio was at last proposed, allowing to gather the data from different configurations.

Acknowledgments

The author would like to acknowledge the financial assistance provided by the China Scholarship Council. We also acknowledge the support for this work from the CNRS research federation FERMaT.

Nomenclature

Latin letters

Symbol	Description	SI Units
a	Interfacial area per unit cell	[m^{-1}]
A	Absorbance	[-]
$C^*_{O_2}$	Oxygen concentration at saturation in the liquid phase	[$kg \cdot m^{-3}$]
$\overline{C_{O_2}}$	Average equivalent oxygen concentration in the liquid slug	[$kg \cdot m^{-3}$]
$C_{\max}$	Maximum oxygen concentration	[$kg \cdot m^{-3}$]
d_h	Channel hydraulic diameter	[m]
E	Chemical enhancement factor	[-]
f_c	Frequency of recirculation in the liquid slug ($f_c \approx U_B / 4L_S$)	[s^{-1}]
I	Intensity, i.e., gray value	[-]
k_2	Reaction rate constant	[$L \cdot mol^{-1} s^{-1}$]
k_L	Liquid side mass transfer coefficient	[$m \cdot s^{-1}$]
L_S	Liquid slug length	[m]
j_{G0}	Superficial velocity of the gas phase ($j_{G0} = Q_{G0}/\Omega$)	[$m \cdot s^{-1}$]
j_L	Superficial velocity of the liquid phase ($j_L = Q_L/\Omega$)	[$m \cdot s^{-1}$]
j_{TP}	Total superficial velocity for two phase flow ($j_{TP}=j_{G0}+j_L$)	[$m \cdot s^{-1}$]
M_{O2}	Molar mass of oxygen	[$kg \cdot mol^{-1}$]
M_{RZ}	Molar mass of resazurin	[$kg \cdot mol^{-1}$]
m	mass	[kg]
S_B	Bubble surface area	[m^2]
t	Time	[s]
U_B	Bubble velocity	[$m \cdot s^{-1}$]
X	Axial position along the spiral tube from the bubble formation point	[m]
x	x axis in Cartesian coordinates	[m]
y	y axis in Cartesian coordinates	[m]
z	z axis in Cartesian coordinates	[m]

Greek symbols

ζ	Coefficient, Eq. (7)	[kg· m^{-4}]
η_0	Ratio of the superficial velocities of the gas and the liquid phases, $\eta_0 = j_{G0}/j_L$	[-]
λ	curvature ratio, defined as $\lambda = 2r/d_{it}$	[-]
μ	Dynamic viscosity of the phase	[Pa· s]
Ω	Cross-sectional area of the channel ($\Omega = {d_h}^2$)	[m^2]
ρ	Density of the phase	[kg· m^{-3}]
φ_{O_2}	Mass flux density of oxygen transferred per unit of area	[kg·m^{-2}·s^{-1}]
ω	Linear dimensionless coefficient associating $k_L\,a$ and f_c	[-]

Dimensionless numbers

Two-phase Capillary number	$\mathrm{Ca}_{TP} = \frac{\mu_L j_{TP}}{\sigma_L}$
Hatta number	$Ha = \frac{\sqrt{k_2\, C_{DH,0}\, D_{O2}}}{k_L}$
Two-phase Reynolds number	$\mathrm{Re}_{TP} = \frac{\rho_L j_{TP} d_h}{\mu_L}$
Two-phase Weber number	$\mathrm{We}_{TP} = \frac{\rho_L\, {j_{TP}}^2\, d_h}{\sigma_L}$

Abbreviations

DH	Dihydroresorufin
fps	Frames per second
MAPER	Mean absolute percentage error of regression
PMMA	Poly-Methyl-Methacrylate
RZ	Resazurin
RF	Resorufin
RGN	Resazurin, Glucose, NaOH colorimetric solution
ROI	Region-of-interest
SD	Standard deviation error
[]	Concentration

Subscripts and Superscripts

exp	Experimental data
G	Gas phase
L	Liquid phase
pre	Predicted data
rl	real
TP	Two-phase flow

Declaration of Competing Interest

The authors report no declarations of interest.

REFERENCES

Abiev, , R.S., Butler, C., Cid, E., Lalanne, B., Billet, A.M., 2019. Mass transfer characteristics and concentration field evolution for gas-liquid Taylor flow in milli channels. Chemical Engineering Science 207, 1331-1340. https://doi.org/10.1016/j.ces.2019.07.046

Abiev, R.S., 2020. Gas-Liquid and Gas-Liquid-Solid mass transfer model for Taylor flow in micro (milli) channels: a theoretical approach and experimental proof. Chemical Engineering Journal Advances, 100065. https://doi.org/10.1016/j.ceja.2020.100065

Bai, L., Zhao, S., Fu, Y., Cheng, Y., 2016. Experimental study of mass transfer in water/ionic liquid microdroplet systems using micro-LIF technique. Chemical Engineering Journal 298, 281-290. https://doi.org/10.1016/j.cej.2016.04.034

Boden, S., Rolo, T.D.S., Baumbach, T., Hampel, U., 2014. Synchrotron radiation microtomography of Taylor bubbles in capillary two-phase flow. Experiments in Fluids 55, 1-14. https://doi.org/10.1007/s00348-014-1768-7

Butler, C., Cid, E., Billet, A.-M., 2016. Modelling of mass transfer in Taylor flow: Investigation with the PLIF-I technique. Chemical Engineering Research and Design 115, 292-302.

Dang, M., Yue, J., Chen, G., Yuan, Q., 2013. Formation characteristics of Taylor bubbles in a microchannel with a converging shape mixing junction. Chemical Engineering Journal 223, 99-109. https://doi.org/10.1016/j.cej.2013.02.108

Dietrich, N., Loubière, K., Jimenez, M., Hébrard, G., Gourdon, C., 2013. A new direct technique for visualizing and measuring gas–liquid mass transfer around bubbles moving in a straight millimetric square channel. Chemical Engineering Science 100, 172-182. https://doi.org/10.1016/j.ces.2013.03.041

Fries, D.M., Trachsel, F., von Rohr, P.R., 2008. Segmented gas–liquid flow characterization in rectangular microchannels. International Journal of Multiphase Flow 34, 1108-1118. https://doi.org/10.1016/j.ijmultiphaseflow.2008.07.002

Fries, D.M., Rohr, P.R.V., 2009. Impact of inlet design on mass transfer in gas–liquid rectangular microchannels. Microfluidics and Nanofluidics 6, 27-35. https://doi.org/10.1007/s10404-008-0292-6

Fu, T., Ma, Y., 2015. Bubble formation and breakup dynamics in microfluidic devices: A review. Chemical Engineering Science 135, 343-372. https://doi.org/10.1016/j.ces.2015.02.016

Garstecki, P., Fuerstman, M.J., Stone, H.A., Whitesides, G.M., 2006. Formation of droplets and bubbles in a microfluidic T-junction - scaling and mechanism of break-up.

Lab on a Chip 6, 437-446. https://doi.org/10.1039/b510841a

Geng, Y., Ling, S., Huang, J., Xu, J., 2020. Multiphase Microfluidics: Fundamentals, Fabrication, and Functions. Small 16, e1906357. https://doi.org/10.1002/smll.201906357

Haase, S., Bauera, T., Hilpmanna, G., Langea, M., Ayubia, M., Abievb, R., 2020. Simultaneous Detection of Hydrodynamics, Mass Transfer and Reaction Rates in a Three-Phase Microreactor. Theoretical Foundations of Chemical Engineering 54, 48-63. https://doi.org/10.1134/S0040579520010091

Higbie, R., 1935. The rate of absorption of a pure gas into a still liquid during short periods of exposure. Trans. AIChE 31, 365–389.

Hoppe, C., 2019. Determination of the reaction constant of resorufin for the examination of oxygen gas-liquid mass transfer, Master-Thesis, Otto-von-Guericke-Universität Magdeburg, , Master-Thesis, Otto-von-Guericke-Universität Magdeburg.

Kastens, S., Timmermann, J., Strassl, F., Rampmaier, R.F., Hoffmann, A., Herres-Pawlis, S., Schlüter, M., 2017. Test System for the Investigation of Reactive Taylor Bubbles. Chemical Engineering & Technology 40, 8.

Kexel, F., von Kameke, A., Tenhaus, J., Hoffmann, M., Schlüter, M., 2021. Taylor Bubble Study of the Influence of Fluid Dynamics on Yield and Selectivity in Fast Gas-Liquid Reactions Chemie Ingenieur Technik n/a. https://doi.org/https://doi.org/10.1002/cite.202000241

Krieger, W., Hörbelt, M., Schuster, S., Hennekes, J., Kockmann, N., 2019. Kinetic study of leuco-indigo carmine oxidation and investigation of Taylor and Dean flow superposition in a coiled flow inverter. Chemical Engineering & Technology 42, 2052-2060. https://doi.org/10.1002/ceat.201800753

Liu, Y., Chen, G., Yue, J., 2020. Manipulation of gas-liquid-liquid systems in continuous flow microreactors for efficient reaction processes. Journal of Flow Chemistry 10, 103-121. https://doi.org/10.1007/s41981-019-00062-9

Liu, Y., Zhao, Q., Yue, J., Yao, C., Chen, G., 2021. Effect of mixing on mass transfer characterization in continuous slugs and dispersed droplets in biphasic slug flow microreactors. Chemical Engineering Journal 406, 126885. https://doi.org/https://doi.org/10.1016/j.cej.2020.126885

Mariotti, A., Antognoli, M., Galletti, C., Mauri, R., Salvetti, M.V., Brunazzi, E., 2020. The role of flow features and chemical kinetics on the reaction yield in a T-shaped micro-reactor. Chemical Engineering Journal, 125223. https://doi.org/10.1016/j.cej.2020.125223

Mei, M., Felis, F., Dietrich, N., Hébrard, G., Loubière, L., 2020a. Hydrodynamics

of gas-liquid slug flows in a long in-plane spiral-shaped milli-reactor. Theoretical Foundations of Chemical Engineering 54, 25-47. https://doi.org/10.1134/S0040579520010169

Mei, M., Hébrard, G., Dietrich, N., Loubière, K., 2020b. Gas-liquid mass transfer around Taylor bubbles flowing in a long, in-plane, spiral-shaped milli-reactor. Chemical Engineering Science 222, 115717. https://doi.org/10.1016/j.ces.2020.115717

Paul, M., Strassl, F., Hoffmann, A., Hoffmann, M., Schlüter, M., Herres-Pawlis, S., 2018. Reaction systems for bubbly flows. European Journal of Inorganic Chemistry 2018, 2101-2124. https://doi.org/https://doi.org/10.1002/ejic.201800146

Roudet, M., Loubiere, K., Gourdon, C., Cabassud, M., 2011. Hydrodynamic and mass transfer in inertial gas-liquid flow regimes through straight and meandering millimetric square channels. Chemical Engineering Science 66, 2974-2990. https://doi.org/10.1016/j.ces.2011.03.045

Sattari-Najafabadi, M., Esfahany, M.N., Wu, Z., Sundén, B., 2017. Hydrodynamics and mass transfer in liquid-liquid non-circular microchannels: comparison of two aspect ratios and three junction structures. Chemical Engineering Journal 322, 328-338.

Schlüter, M., Kexel, F., von Kameke, A., Hoffmann, M., Herres-Pawlis, S., Klüfers, P., Oßberger, M., Turek, S., Mierka, O., Kockmann, N., Krieger, W., 2021. Visualization and Quantitative Analysis of Consecutive Reactions in Taylor Bubble Flows, Fluid Mechanics and its Applications, pp. 507-543.

Soh, G.Y., Yeoh, G.H., Timchenko, V., 2017. A CFD model for the coupling of multiphase, multicomponent and mass transfer physics for micro-scale simulations. International Journal of Heat and Mass Transfer 113, 922-934. https://doi.org/10.1016/j.ijheatmasstransfer.2017.06.001

Sun, R., Cubaud, T., 2011. Dissolution of carbon dioxide bubbles and microfluidic multiphase flows. Lab on a Chip 11, 2924.

Svetlov, S.D., Abiev, R.S., 2021. Mathematical modeling of the droplet formation process in a microfluidic device. Chemical Engineering Science, 116493. https://doi.org/10.1016/j.ces.2021.116493

Tan, J., Lu, Y.C., Xu, J.H., Luo, G.S., 2012. Mass transfer characteristic in the formation stage of gas-liquid segmented flow in microchannel. Chemical Engineering Journal 185, 314-320. https://doi.org/10.1016/j.cej.2012.01.054

Willms, T., Kryk, H., Hampel, U., 2019. Microreactor studies for efficient organic oxidation processes. Catalysis Today. https://doi.org/10.1016/j.cattod.2019.05.008

Xu, F., Yang, L., Liu, Z., Chen, G., 2021. Numerical investigation on the hydrodynamics of Taylor flow in ultrasonically oscillating microreactors. Chemical

Engineering Science, 116477. https://doi.org/10.1016/j.ces.2021.116477

Xu, J.H., Tan, J., Li, S.W., Luo, G.S., 2008. Enhancement of mass transfer performance of liquid–liquid system by droplet flow in microchannels. Chemical Engineering Journal 141, 242-249. https://doi.org/10.1016/j.cej.2007.12.030

Yan, Z., Tian, J., Wang, K., Nigam, K.D.P., Luo, G., 2021. Microreaction processes for synthesis and utilization of epoxides: A review. Chemical Engineering Science 229, 116071. https://doi.org/10.1016/j.ces.2020.116071

Yang, L., Dietrich, N., Loubière, K., Gourdon, C., Hébrard, G., 2016a. Visualization and characterization of gas-liquid mass transfer around a Taylor bubble right after the formation stage in microreactors. Chemical Engineering Science 143, 364-368. https://doi.org/10.1016/j.ces.2016.01.013

Yang, L., Dietrich, N., Loubière, K., Gourdon, C., Hébrard, G., 2016b. Optical methods to investigate the enhancement factor of an oxygen-sensitive colorimetric reaction using microreactors. AIChE Journal. https://doi.org/10.1002/aic.15547

Yang, L., Loubière, K., Dietrich, N., Men, C.L., Gourdon, C., Hébrard, G., 2017. Local investigations on the gas-liquid mass transfer around Taylor bubbles flowing in a meandering millimetric square channel. Chemical Engineering Science 165, 192-203. https://doi.org/10.1016/j.ces.2017.03.007

Yang, L., Xu, F., Chen, G., 2022. Enhancement of gas-liquid mass transfer and mixing in zigzag microreactor under ultrasonic oscillation. Chemical Engineering Science 247, 117094. https://doi.org/https://doi.org/10.1016/j.ces.2021.117094

Yao, C., Dong, Z., Zhao, Y., Chen, G., 2014. An online method to measure mass transfer of slug flow in a microchannel. Chemical Engineering Science 112, 15-24. https://doi.org/10.1016/j.ces.2014.03.016

Yao, C., Dong, Z., Zhao, Y., Chen, G., 2015. Gas-liquid flow and mass transfer in a microchannel under elevated pressures. Chemical Engineering Science 123, 137-145.

Yao, C., Zhao, Y., Ma, H., Liu, Y., Zhao, Q., Chen, G., 2021. Two-phase flow and mass transfer in microchannels: A review from local mechanism to global models. Chemical Engineering Science 229, 116017. https://doi.org/https://doi.org/10.1016/j.ces.2020.116017

Zhang, Peng, Yao, C., Ma, H., Jin, N., Zhang, X., Lü, H., Zhao, Y., 2018. Dynamic changes in gas-liquid mass transfer during Taylor flow in long serpentine square microchannels. Chemical Engineering Science 182, 17-27. https://doi.org/10.1016/j.ces.2018.02.018

Zhang, Y., Zhang, X., Xu, B., Cai, W., Wang, F., 2015. CFD simulation of mass transfer intensified by chemical reactions in slug flow microchannels. The Canadian

Journal of Chemical Engineering 93, 2307-2314. https://doi.org/10.1002/cjce.22360

Zhao, Q., Ma, H., Liu, Y., Yao, C., Yang, L., Chen, G., 2021. Hydrodynamics and mass transfer of Taylor bubbles flowing in non-Newtonian fluids in a microchannel. Chemical Engineering Science 231, 116299. https://doi.org/10.1016/j.ces.2020.116299